Article

Durable CO_2 conversion in the proton-exchange membrane system

https://doi.org/10.1038/s41586-023-06917-5

Received: 4 September 2022

Accepted: 30 November 2023

Published online: 31 January 2024

Check for updates

Wensheng Fang[1,10], Wei Guo[1,10], Ruihu Lu[2,10], Ya Yan[3], Xiaokang Liu[4], Dan Wu[4], Fu Min Li[1], Yansong Zhou[1], Chaohui He[1], Chenfeng Xia[1], Huiting Niu[1], Sicong Wang[4], Youwen Liu[5], Yu Mao[2], Chengyi Zhang[2], Bo You[1], Yuanjie Pang[6], Lele Duan[7], Xuan Yang[1], Fei Song[8], Tianyou Zhai[5], Guoxiong Wang[9], Xingpeng Guo[1], Bien Tan[1], Tao Yao[4]✉, Ziyun Wang[2]✉ & Bao Yu Xia[1]✉

Electrolysis that reduces carbon dioxide (CO_2) to useful chemicals can, in principle, contribute to a more sustainable and carbon-neutral future[1–6]. However, it remains challenging to develop this into a robust process because efficient conversion typically requires alkaline conditions in which CO_2 precipitates as carbonate, and this limits carbon utilization and the stability of the system[7–12]. Strategies such as physical washing, pulsed operation and the use of dipolar membranes can partially alleviate these problems but do not fully resolve them[11,13–15]. CO_2 electrolysis in acid electrolyte, where carbonate does not form, has therefore been explored as an ultimately more workable solution[16–18]. Herein we develop a proton-exchange membrane system that reduces CO_2 to formic acid at a catalyst that is derived from waste lead–acid batteries and in which a lattice carbon activation mechanism contributes. When coupling CO_2 reduction with hydrogen oxidation, formic acid is produced with over 93% Faradaic efficiency. The system is compatible with start-up/shut-down processes, achieves nearly 91% single-pass conversion efficiency for CO_2 at a current density of 600 mA cm^{-2} and cell voltage of 2.2 V and is shown to operate continuously for more than 5,200 h. We expect that this exceptional performance, enabled by the use of a robust and efficient catalyst, stable three-phase interface and durable membrane, will help advance the development of carbon-neutral technologies.

The major issue of carbonate precipitation hinders the development of efficient and scalable CO_2 conversion[7,11,19,20], as shown in the calculated Pourbaix diagram (Fig. 1a), carbonate formation occurs over a wide pH range. Therefore, to avoid carbonate formation in formic acid production, the CO_2 reduction reaction (CO_2RR) in a strong acid operated under a proton-exchange membrane (PEM) system is believed to be among potential solutions, by taking advantage of state-of-the-art water electrolysis and finally solving the carbonate precipitation problem[16–18]. We developed a PEM electrolyser for acid CO_2 electrolysis in which the hydrogen oxidation reaction (HOR) occurs at the anode and CO_2 is converted directly to formic acid at the cathode (Fig. 1b). The cathode recycled Pb (r-Pb) catalyst is obtained from lead–acid battery waste, which can be prepared industrially at the kilogram—or even ton—scale (Fig. 1c, inset). This r-Pb catalyst is a composite of lead and lead sulfate (Pb–$PbSO_4$), as shown by its X-ray diffraction (XRD) pattern (Fig. 1c and Supplementary Fig. 1)[21]. Field-emission scanning electron microscopy shows that the particle size of r-Pb can be controlled, from micrometre to nanometre, by adjustment of ball-milling time (Fig. 1d and Supplementary Figs. 2–4). Cryo-electron microscopy observation showed two lattice fringes, of 0.21 and 0.29 nm and attributed to $PbSO_4$ and Pb, respectively (Fig. 1e and Supplementary Fig. 5a–e). Energy-dispersive X-ray spectroscopy mapping further verified the presence of Pb, C, O and S (Supplementary Fig. 5f–h). Fourier transform infrared spectroscopy (FTIR) showed a characteristic sulfate peak at 1,100 cm^{-1} (Supplementary Fig. 6a). Moreover, X-ray photoelectron spectroscopy (XPS) demonstrated the typical signals of C 1*s*, O 1*s*, S 2*p* and Pb 4*f* in the r-Pb composite (Supplementary Fig. 6b–f).

We then evaluated the electrochemical activity of the cathodic CO_2RR over the r-Pb catalyst in a PEM electrolyser (pH 1.0) coupled with the anodic HOR (Supplementary Fig. 7). As shown in Fig. 2a, the optimized electrode, produced by adjustment of milling time, showed a formic acid Faradaic efficiency of over 93% and achieved

[1]School of Chemistry and Chemical Engineering, State Key Laboratory of Materials Processing and Die & Mould Technology, Key Laboratory of Material Chemistry for Energy Conversion and Storage (Ministry of Education), Hubei Key Laboratory of Material Chemistry and Service Failure, Wuhan National Laboratory for Optoelectronics, Huazhong University of Science and Technology, Wuhan, China. [2]School of Chemical Sciences, University of Auckland, Auckland, New Zealand. [3]CAS Key Laboratory of Materials for Energy Conversion, Shanghai Institute of Ceramics, Chinese Academy of Sciences, Shanghai, China. [4]National Synchrotron Radiation Laboratory, University of Science and Technology of China, Hefei, China. [5]State Key Laboratory of Materials Processing and Die & Mould Technology and School of Materials Science and Engineering, Huazhong University of Science and Technology, Wuhan, China. [6]School of Optical and Electronic Information, Wuhan National Laboratory for Optoelectronics, Huazhong University of Science and Technology, Wuhan, China. [7]Department of Chemistry and Shenzhen Grubbs Institute, Southern University of Science and Technology, Shenzhen, China. [8]Shanghai Synchrotron Radiation Facility, Shanghai Advanced Research Institute, Chinese Academy of Sciences, Shanghai, China. [9]State Key Laboratory of Catalysis, Dalian National Laboratory for Clean Energy, Dalian Institute of Chemical Physics, Chinese Academy of Sciences, Dalian, China. [10]These authors contributed equally: Wensheng Fang, Wei Guo, Ruihu Lu. ✉e-mail: yaot@ustc.edu.cn; ziyun.wang@auckland.ac.nz; byxia@hust.edu.cn

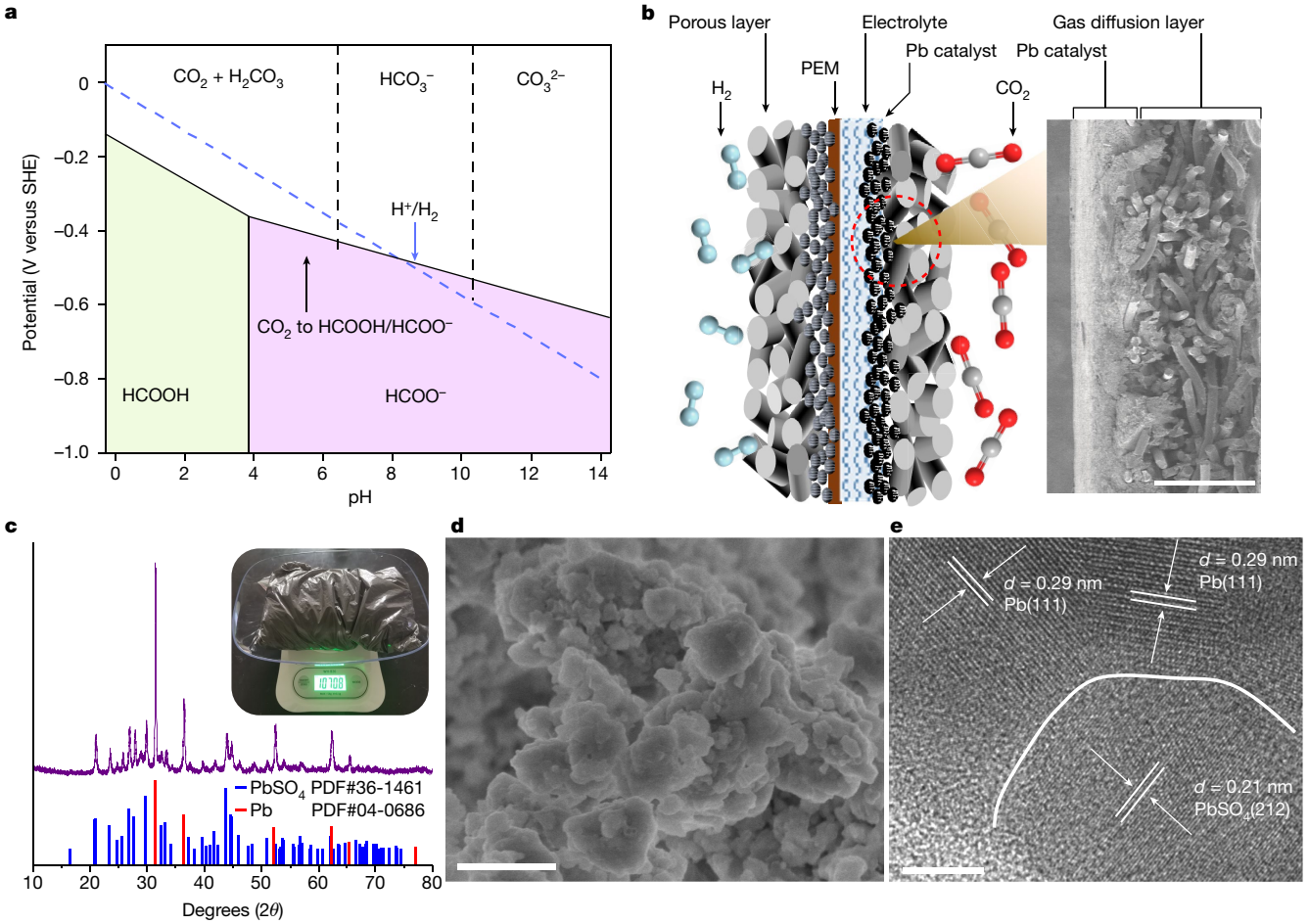

Fig. 1 | Physical characterization. a, Pourbaix diagram of formic acid and hydrogen generation in CO_2RR (H_2CO_3 $K^{\ominus}_{a1} = 4.2 \times 10^{-7}$; $K^{\ominus}_{a2} = 4.7 \times 10^{-11}$; SHE, standard hydrogen electrode; $K^{\ominus}_{a1}$ and $K^{\ominus}_{a2}$ are the first and second dissociation equilibrium constants of carbonic acid, respectively). **b**, Schematic diagram of a PEM electrolyser used for CO_2RR. Right, cross-sectional SEM image of a fabricated cathode electrode. **c**–**e**, XRD pattern (**c**), SEM (**d**) and TEM (**e**) images of the r-Pb catalyst. Inset in **c** is a digital image of the r-Pb catalyst obtained from a waste lead–acid battery. Scale bars, 100 μm (**b**), 500 nm (**d**), 5 nm (**e**); *d* is the lattice spacing.

a high current density of 1.2 A cm^{-2} at a cell voltage of 2.4 V (Supplementary Fig. 8 and Supplementary Table 1). We also found a nearly identical potassium cationic effect on CO_2RR, as reported in the literature (Supplementary Fig. 9)[9,22]. The r-Pb electrode showed excellent pH tolerance, with a high Faradaic efficiency of 64% at pH 0 (due to excessive HER kinetics) and over 91% at all other pH values (Fig. 2b and Supplementary Fig. 10). In alkaline electrolyte (pH 14.0), however, the carbonate precipitation problem resulted in a significant carbon loss of 50% whereas the acid PEM system achieved a very low carbon loss of less than 1% (Fig. 2b and Supplementary Fig. 11)[23]. Moreover, a high single-pass conversion efficiency of around 91% for CO_2 was realized by optimization of CO_2 gas flow rate to 3 standard cubic centimetres min^{-1} (sccm) in this PEM device (Fig. 2c and Supplementary Fig. 12). More importantly, the device can be stably operated for 5,200 h at 2.2 V and current density of 600 mA cm^{-2} (Fig. 2d). The outstanding stability demonstrated by our PEM system can primarily be attributed to the chemically stable r-Pb catalyst, which had survived in lead–acid batteries for tens of thousands of hours. This r-Pb catalyst also showed virtually unattenuated chemical stability even after 300 days (Fig. 2e) and has excellent compatibility with practical operations involving start-up/shut-down (Fig. 2e, inset)[24]. Moreover, the electrolyte overflow induced by electrowetting of the three-phase interface often results in system failure[25,26]. Herein, the stability of the three-phase interface was maintained by reprocessing the gas diffusion electrode using a polytetrafluoroethylene (PTFE) emulsion every 200 h (Fig. 2f and Supplementary Figs. 13–16). In addition, we also achieved 2,000 h stability without any reprocessing operation by PTFE membrane-supported r-Pb catalysts (Supplementary Figs. 17–19). Furthermore, the anode reaction plays an essential role in the whole system, affecting cell voltage, reaction rate, product distribution, membrane stability and system life[27,28]. By utilization of HOR rather than the water oxidation reaction (WOR) at the anode, we were able to decrease the overall voltage and, more importantly, avoid the generation of harmful hydrogen peroxide that could degrade and even destroy the PEM[28–30]. This ultimately contributed to the durable membrane and long service life of the PEM system (Fig. 2g and Supplementary Figs. 20–23). In addition, techno-economic analysis (TEA) showed the feasibility of our system using HOR at the anode compared with the WOR strategy (Supplementary Figs. 24 and 25 and Supplementary Table 2). When employing renewable power from onshore wind as the driving force, we can achieve a higher economic profit per ton of formic acid (Supplementary Fig. 26 and Supplementary Tables 2 and 3)[27,31,32]. Following simple rotary evaporation, the electrolyte can be recycled to the catholyte and a formic acid solution (2 M) obtained (Supplementary Fig. 27). No Pb leakage was found in the electrolyte during chemical and electrochemical operations (Supplementary Table 4). Therefore, a PEM reactor of area 5 × 5 cm^2 could achieve a current of 15 A at a voltage of roughly 2.7 V with Faradaic efficiency

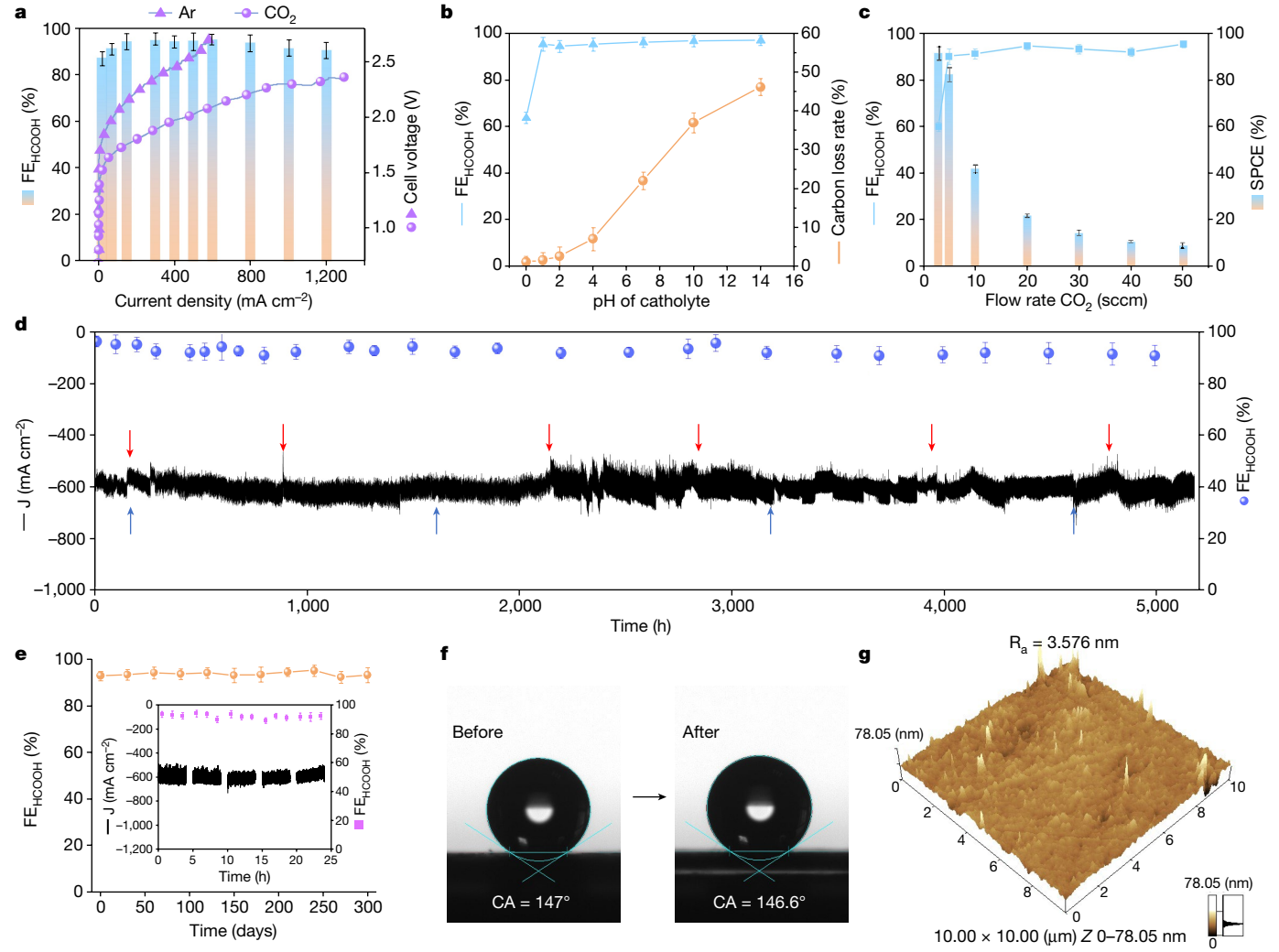

Fig. 2 | Electrochemical measurements. a, Linear sweep voltammetry (LSV) curves of r-Pb under CO_2 and Ar atmospheres in an acid PEM electrolyser, and Faradaic efficiency (FE) of CO_2RR to formic acid on r-Pb at varying current density. **b**, Faradaic efficiency of formic acid and corresponding carbon loss rate at a current density of 600 mA cm^{-2} for variable pH. **c**, Single-pass conversion efficiency (SPCE) of the r-Pb catalyst under varying CO_2 flow rate. **d**, Electrochemical stability of the PEM reactor at a cell voltage of 2.2 V. Positions indicated by red and blue arrows represent those of replacement of electrolyte and reaction gas, respectively. **e**, Chemical stability of the r-Pb catalyst recorded at 600 mA cm^{-2} in the PEM reactor. Inset, the stability test consisting of start-up/shut-down experiments. **f**, Contact angle (CA) measurements of the gas diffusion electrode before and after CO_2 electrolysis at 2.2 V for 2,000 h. **g**, Atomic force microscopy image of the PEM following 500 h of electrolysis in the PEM system at 2.2 V. Error bars represent the standard deviation of measurements based on three independent samples. R_a in Fig. 2g represents the average roughness.

of over 91% for formic acid generation, demonstrating the scalability of the PEM system (Supplementary Fig. 28).

The r-Pb electrode undergoes structural transformation from Pb–$PbSO_4$ to Pb–$PbCO_3$ during CO_2 electrolysis (Fig. 3a and Supplementary Fig. 29). Scanning electron microscope (SEM) images suggest the formation and element distribution of flake-like stacking of structured $PbCO_3$ (Fig. 3b and Supplementary Fig. 30a–c). Transmission electron microscopy (TEM) images show the internal structure of the catalyst, exhibiting a mixture of Pb and $PbCO_3$ (Supplementary Fig. 30d–f). XPS results also demonstrate carbonate formation in the electrode following the reactions (Supplementary Fig. 31)[33]. In situ XRD and Raman characterization confirm that structural transformation is related to the reaction process rather than the applied voltage (Fig. 3c,d and Supplementary Figs. 32 and 33). A major Raman peak at 977 cm^{-1} assigned to $PbSO_4$ gradually weakened and disappeared, accompanied by peak emergence at 1,055 cm^{-1} assigned to carbonate during 1,800 s of CO_2 electrolysis (Fig. 3d)[33]. Soft X-ray absorption spectroscopy then showed that the state of oxygen had changed distinctly along with CO_2RR (Supplementary Fig. 34), initially from a flat line to a distinct peak over a short period of time and then stabilized at 534 eV, assigned to $PbCO_3$. In situ extended X-ray absorption fine-structure (EXAFS) measurements at the Pb L_3 edge were performed to investigate the chemical state of Pb under working conditions. X-ray absorption near-edge structure (XANES) profiles indicate that the valence state of Pb gradually decreased (Fig. 3e). With increasing applied potential, from −1.3 to −1.7 V versus reversible hydrogen electrode (RHE), the absorption edges showed a low-energy shift, indicating that the valence state of Pb had gradually decreased under working conditions. Moreover, the positions of all absorption edges were higher than that of Pb foil, indicating that the valence of Pb remained above zero, further confirmed by EXAFS. As shown in Fig. 3f, four dominant peaks can be seen in all spectra obtained at varying applied potential. The two peaks located at 1.5 and 2.2 Å correspond to Pb-O/C in PbO, $PbCO_3$ and $PbSO_4$ whereas the other two, at 2.7 and 3.4 Å, belong to Pb–Pb in metallic Pb. With the applied potential increasing from −1.3 to −1.7 V, Pb-O/C peaks decreased while Pb–Pb peaks increased, indicating an increasing percentage of metallic Pb. Furthermore, the location of the characteristic peaks at approximately 2.2 Å showed a high redshift tendency, which

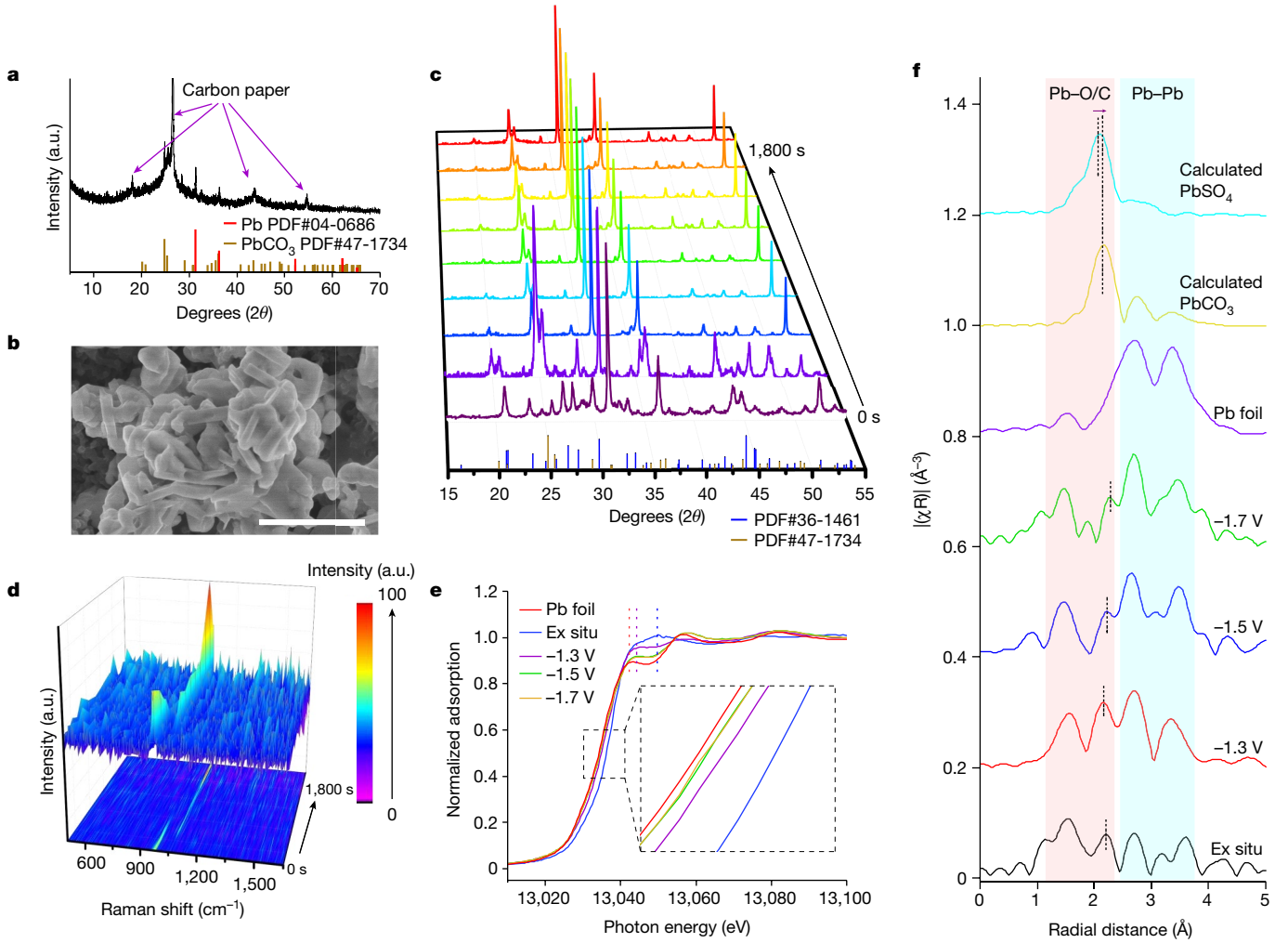

Fig. 3 | In situ characterization. a,**b**, XRD pattern (**a**) and SEM image (**b**) of the r-Pb catalyst following CO_2 reduction for 100 h. **c**,**d**, In situ XRD profiles (**c**) and Raman spectra (**d**) of the r-Pb catalyst at −1.7 V versus RHE. **e**,**f**, In situ XANES spectra recorded at the Pb L_3-edge on the r-Pb catalyst at varying applied potential (versus RHE) (**e**) and corresponding Fourier-transformed k^2-weighted EXAFS spectra along with the calculated $PbSO_4$ and $PbCO_3$ spectra as references (**f**). Inset in **e** shows the magnified absorption edge of the XANES region. Scale bar, 500 nm. a.u., arbitrary units. 'Ex situ' in panels **e** and **f** represents the curve obtained at open-circuit potential.

demonstrates the structural change from $PbSO_4$ to $PbCO_3$ by combining previous electrochemical data results. In summary, in situ XAFS characterization confirmed the coexistence and gradual evolution of Pb(II) and metallic Pb on the r-Pb electrode and further illustrated the dynamic structural transformation from Pb–$PbSO_4$ to the Pb–$PbCO_3$ composite during CO_2 electrolysis. A similar structural transformation was also observed for other catalysts, indicating that the catalytic structure of the Pb–$PbCO_3$ composite is thermodynamically stable in our PEM system (Supplementary Fig. 35). Our experiments exploring the reaction behaviour of r-Pb in H-cells and flow cells also yielded different results (Supplementary Fig. 36). The Tafel slope value (approximately 60 mV dec^{-1}) for different catalysts indicates the identical accelerated kinetics of CO_2RR in flow cells (Supplementary Fig. 37)[34,35]. These findings offer significant insight into the dynamic behaviours of the r-Pb catalyst, emphasizing the importance of comprehending the structure–function relationship when designing efficient catalysts for CO_2 electrolysis.

To track the carbon path in CO_2 electrolysis, we employed C isotope-tracing experiments on $Pb^{13}CO_3$ and $^{13}CO_2$ (Supplementary Figs. 38 and 39). Except for $H^{12}COOH$, a small amount of $H^{13}COOH$ was observed in the $^{12}CO_2$ reduction on $Pb^{13}CO_3$ during the initial 30 h of electrolysis (Supplementary Fig. 40a). However, after switching $^{13}CO_2$ and $^{12}CO_2$ gas on $Pb^{13}CO_3$ ($^{13}CO_2$ replaced $^{12}CO_2$ in the first cycle and $^{12}CO_2$ replaced $^{13}CO_2$ in the second), $H^{12}COOH$ and $H^{13}COOH$ successively appeared (Supplementary Fig. 40b–d). A further C isotope-tracing experiment using $^{13}CO_2$ reduction on $Pb^{12}CO_3$ showed the same phenomenon (Supplementary Fig. 40e–g). Moreover, high-resolution liquid mass spectrometry verified that C in the labelled CO_2 was also included in the catalyst composite (Supplementary Fig. 41a–c). In addition, the results of ^{18}O-labelled $^{12}C^{18}O_2$ reduction on $Pb^{12}C^{16}O_3$ also confirmed that both O and C in the entire CO_2 molecule are involved in both this phase transformation and CO_2RR (Supplementary Fig. 41d,e). The total amount of $H^{13}COOH$ produced from $^{12}CO_2$ electrolysis on $Pb^{13}CO_3$ was about 210 nmol following 60 h of electrolysis, suggesting that around 6 wt% of carbon in the composite electrode had participated in this CO_2RR, which is equivalent to around one or two layers of carbonate in the catalytic reaction (Supplementary Fig. 41f). In situ synchrotron radiation Fourier transform infrared (SR–FTIR) spectra showed two pronounced, stable peaks at 1,396 and 1,650 cm^{-1} in a broad potential range of around −1.0 to 1.8 V versus RHE, corresponding to HCOO* and H_2O, respectively (Supplementary Fig. 42a,b)[33]. In addition, the peak at 1,396 cm^{-1} persisted over time at −1.7 V versus RHE (Supplementary Fig. 42c). SR–FTIR also showed a blue-shift in the characteristic peak of HCOO* in the isotope-labelled CO_2RR (Supplementary Fig. 42d). All

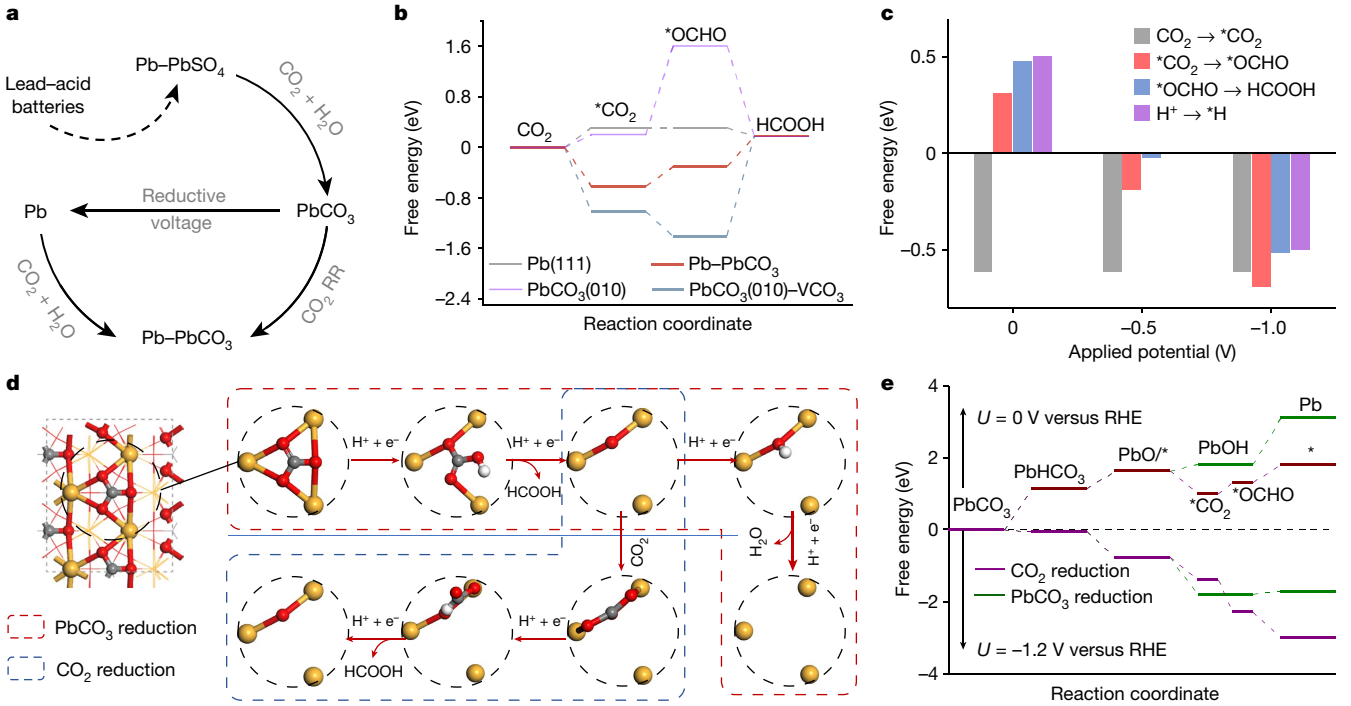

Fig. 4 | Theoretical investigation. a, Schematic phase transition of the r-Pb catalyst. **b**, Free energy profile along the CO_2RR on active Pb atoms, $PbCO_3$(010)-VCO_3 represents a vacancy of carbonate in $PbCO_3$(010). **c**, Free energy changes in reactions under varying applied potential. **d**, Schematic diagram of the solid transformation-induced catalytic mechanism. White, grey, red and orange spheres represent H, C, O and Pb atoms, respectively. **e**, Free energy profile of $PbCO_3$ reduction and CO_2 reduction during phase transition. Asterisk (*) denotes the PbO configuration, which serves as the CO_2RR site; *U* represents the applied potential in the DFT simulation process.

the above results suggest that there is a solid-phase transition and lattice carbon activation mechanism in the CO_2RR on the r-Pb electrode.

We then used density functional theory (DFT) calculation to investigate the high activity and stability of CO_2RR on the r-Pb electrode, specifically focusing on the Pb–$PbCO_3$ interface. Initially we hypothesized the solid-phase transformation of r-Pb from waste lead–acid batteries in the PEM system (Fig. 4a) and identified the main Pb-related species as metallic Pb, $PbCO_3$ and an interface of Pb–$PbCO_3$. Accordingly, the CO_2RR process was investigated on Pb sites with potential locally stable environments (Supplementary Fig 43 and Supplementary Table 5), including metal Pb(111), $PbCO_3$(010), $PbCO_3$–VCO_3 and Pb–$PbCO_3$ interfaces. We found that the CO_2RR starts with a chemical adsorption process followed by electroreduction; we used the O-C-O angle and Pb oxidation state to describe the degree of the chemical and electrochemical processes, respectively (Supplementary Figs. 44 and 45). Due to its strong CO_2 adsorption and chemical activation in the form of a carbonate configuration (Supplementary Fig. 46), Pb–$PbCO_3$ exhibited the lowest free energy upshift for the CO_2RR towards HCOOH, suggesting high theoretical CO_2RR activity (Fig. 4b). Meanwhile, the $*CO_2$ adsorption energies on Pb–$PbCO_3$ were found to be −0.62 eV, favouring CO_2 adsorption rather than *H adsorption. In addition, a moderate energy increase of 0.31 and 0.48 eV for the following two hydrogenation steps, respectively, was lower than that of HER (0.50 eV). This further ensured superior catalytic performance toward the CO_2RR. The Pb–$PbCO_3$ site still prioritized potential-independent $*CO_2$ adsorption compared with *H adsorption, even when the potential reached −1.0 V (Fig. 4c). Electrochemical CO_2RR steps maintained a lower energy change relative to HER, suggesting that the CO_2RR is the dominant reaction compared with HER, enabling the CO_2RR to operate in acidic electrolytes without the need to account for carbonate.

We investigated the site evolution of Pb–$PbCO_3$ during the phase transition of r-Pb (Fig. 4d). The formation energy of $PbHCO_3$ via proton-coupled electron transfer was 1.1 eV, which was the highest along the phase transition. At a working potential of −1.2 V, this step can occur spontaneously from a thermodynamic perspective (Fig. 4e). Subsequently, the PbO(*) configuration was formed with the release of HCOOH following the second hydrogenation, which is in agreement with our observations in the Pourbaix diagram (Supplementary Fig. 47 and Supplementary Tables 6 and 7). It is worth noting that, compared with the third hydrogenation on PbO(*), the CO_2 molecule bound more strongly to PbO(*) and therefore the activation of CO_2 molecules is in the form carbonate on PbO. Next, the two-electron CO_2RR toward HCOOH tended to occur on the PbO(*) site rather than the subsequent $PbCO_3$ reduction toward metallic Pb. This finding suggests that the CO_2RR can avoid $PbCO_3$ reduction, maintaining a stable Pb–$PbCO_3$ interface. Meanwhile, metallic Pb can be converted spontaneously to $PbCO_3$ with the flow of CO_2 and electrolyte[36]. A Pb–$PbCO_3$ phase transition cycle (Fig. 4a) dynamically generated active sites of Pb–$PbCO_3$, theoretically guaranteeing the high stability of the r-Pb catalyst for the CO_2RR.

In closing we note that, although we have shown that our PEM system is capable of efficient and stable conversion of CO_2 to formic acid, developing it into a technology that can contribute to a more sustainable and carbon-neutral future will depend critically on the availability of truly renewable and affordable electricity, CO_2 and H_2.

Online content

Any methods, additional references, Nature Portfolio reporting summaries, source data, extended data, supplementary information, acknowledgements, peer review information; details of author contributions and competing interests; and statements of data and code availability are available at https://doi.org/10.1038/s41586-023-06917-5.

1. De Luna, P. et al. What would it take for renewably powered electrosynthesis to displace petrochemical processes? *Science* **364**, eaav3506 (2019).
2. Wang, Z. et al. Carbon-confined indium oxides for efficient carbon dioxide reduction in a solid-state electrolyte flow cell. *Angew. Chem. Int. Ed. Engl.* **61**, e202200552 (2022).
3. Hori, Y. et al. "Deactivation of copper electrode" in electrochemical reduction of CO_2. *Electrochim. Acta* **50**, 5354–5369 (2005).
4. Gao, S. et al. Partially oxidized atomic cobalt layers for carbon dioxide electroreduction to liquid fuel. *Nature* **529**, 68–71 (2016).
5. Zhu, P. & Wang, H. High-purity and high-concentration liquid fuels through CO_2 electroreduction. *Nat. Catal.* **4**, 943–951 (2021).
6. Xue, W. et al. Operando reconstruction towards stable CuI nanodots with favorable facets for selective CO_2 electroreduction to C_2H_4. *Sci. China Chem.* **66**, 1834–1843 (2023).
7. Huang, J. E. et al. CO_2 electrolysis to multicarbon products in strong acid. *Science* **372**, 1074–1078 (2021).
8. Rabinowitz, J. A. & Kanan, M. W. The future of low-temperature carbon dioxide electrolysis depends on solving one basic problem. *Nat. Commun.* **11**, 5231 (2020).
9. Gu, J. et al. Modulating electric field distribution by alkali cations for CO_2 electroreduction in strongly acidic medium. *Nat. Catal.* **5**, 268–276 (2022).
10. Xie, Y. et al. High carbon utilization in CO_2 reduction to multicarbon products in acidic media. *Nat. Catal.* **5**, 564–570 (2022).
11. Ozden, A. et al. Carbon-efficient carbon dioxide electrolysers. *Nat. Sustain.* **5**, 563–573 (2022).
12. Yang, H., Kaczur, J. J., Sajjad, S. D. & Masel, R. I. Performance and long-term stability of CO_2 conversion to formic acid using a three-compartment electrolyzer design. *J. CO_2 Util.* **42**, 101349 (2020).
13. Yan, Z., Hitt, J. L., Zeng, Z., Hickner, M. A. & Mallouk, T. E. Improving the efficiency of CO_2 electrolysis by using a bipolar membrane with a weak-acid cation exchange layer. *Nat. Chem.* **13**, 33–40 (2021).
14. Masel, R. I. et al. An industrial perspective on catalysts for low-temperature CO_2 electrolysis. *Nat. Nanotechnol.* **16**, 118–128 (2021).
15. O'Brien, C. P. et al. Single pass CO_2 conversion exceeding 85% in the electrosynthesis of multicarbon products via local CO_2 regeneration. *ACS Energy Lett.* **6**, 2952–2959 (2021).
16. Oßkopp, M. et al. Producing formic acid at low pH values by electrochemical CO_2 reduction. *J. CO_2 Util.* **56**, 101823 (2022).
17. Li, J. & Kornienko, N. Electrocatalytic carbon dioxide reduction in acid. *Chem. Catal.* **2**, 29–38 (2022).
18. Bondue, C. J., Graf, M., Goyal, A. & Koper, M. T. M. Suppression of hydrogen evolution in acidic electrolytes by electrochemical CO_2 reduction. *J. Am. Chem. Soc.* **143**, 279–285 (2021).
19. Deng, P. et al. Metal-organic framework-derived carbon nanorods encapsulating bismuth oxides for rapid and selective CO_2 electroreduction to formate. *Angew. Chem. Int. Ed. Engl.* **59**, 10807–10813 (2020).
20. Gao, D. et al. Designing electrolyzers for electrocatalytic CO_2 reduction. *Acta Phys. Chim. Sin.* **37**, 2009021 (2021).
21. Lopes, P. P. & Stamenkovic, V. R. Past, present, and future of lead–acid batteries. *Science* **369**, 923–924 (2020).
22. Monteiro, M. C. O. et al. Absence of CO_2 electroreduction on copper, gold and silver electrodes without metal cations in solution. *Nat. Catal.* **4**, 654–662 (2021).
23. Wang, Z. et al. Advanced catalyst design and reactor configuration upgrade in electrochemical carbon dioxide conversion. *Adv. Mater.* https://doi.org/10.1002/adma.202303052 (2023).
24. Endrodi, B. et al. Operando cathode activation with alkali metal cations for high current density operation of water-fed zero-gap carbon dioxide electrolysers. *Nat. Energy* **6**, 439–448 (2021).
25. Wu, Y. et al. Mitigating electrolyte flooding for electrochemical CO_2 reduction via infiltration of hydrophobic particles in a gas diffusion layer. *ACS Energy Lett.* **7**, 2884–2892 (2022).
26. Xing, Z., Hu, L., Ripatti, D. S., Hu, X. & Feng, X. Enhancing carbon dioxide gas-diffusion electrolysis by creating a hydrophobic catalyst microenvironment. *Nat. Commun.* **12**, 136 (2021).
27. Overa, S. et al. Enhancing acetate selectivity by coupling anodic oxidation to carbon monoxide electroreduction. *Nat. Catal.* **5**, 738–745 (2022).
28. Xiao, F. et al. Atomically dispersed Pt and Fe sites and Pt–Fe nanoparticles for durable proton exchange membrane fuel cells. *Nat. Catal.* **5**, 503–512 (2022).
29. Zhang, Z. et al. Conversion of reactive carbon solutions into CO at low voltage and high carbon efficiency. *ACS Cent. Sci.* **8**, 749–755 (2022).
30. Fan, L., Xia, C., Zhu, P., Lu, Y. & Wang, H. Electrochemical CO_2 reduction to high-concentration pure formic acid solutions in an all-solid-state reactor. *Nat. Commun.* **11**, 3633 (2020).
31. Jouny, M., Luc, W. & Jiao, F. General techno-economic analysis of CO_2 electrolysis systems. *Ind. Eng. Chem. Res.* **57**, 2165–2177 (2018).
32. Shin, H., Hansen, K. U. & Jiao, F. Techno-economic assessment of low-temperature carbon dioxide electrolysis. *Nat. Sustain.* **4**, 911–919 (2021).
33. Shi, Y. et al. Unveiling hydrocerussite as an electrochemically stable active phase for efficient carbon dioxide electroreduction to formate. *Nat. Commun.* **11**, 3415 (2020).
34. Lee, C. H. & Kanan, M. W. Controlling H^+ vs CO_2 reduction selectivity on Pb electrodes. *ACS Catal.* **5**, 465–469 (2014).
35. Chen, Y., Li, C. W. & Kanan, M. W. Aqueous CO_2 reduction at very low overpotential on oxide-derived Au nanoparticles. *J. Am. Chem. Soc.* **134**, 19969–19972 (2012).
36. Zhang, Z. et al. Revealing structural evolution of PbS nanocrystal catalysts in electrochemical CO_2 reduction using in situ synchrotron radiation X-ray diffraction. *J. Mater. Chem. A* **7**, 23775–23780 (2019).

Methods

Materials

Anhydrous ethanol, potassium hydroxide (KOH), potassium sulfate (K_2SO_4) and sulfuric acid (H_2SO_4, about 98%) were purchased from Sinopharm Chemical Reagent Co., Ltd. Platinum ruthenium black (Pt 50%, Ru 50%) was purchased from Aladdin. SaiKeSaiSi (SKSS) comprised PtIrRu and was purchased from Success-Bio-Tech Co., Ltd. Both 480 and 520, supported on carriers TiO_2 and NbO_x and with Ir content of 75 wt%, were purchased from Umicore Group. TANAKA (TKK) comprises IrO_x and was purchased from Tanaka. Carbon nanotube, acetylene black, PTFE emulsion (60 wt%), PTFE membrane and ketjen black were purchased from Aladdin. Sodium naphthalene treatment solution was purchased from Huiju Glue. All reagents were used without further purification. The lead–acid battery was purchased from XinshenshiI, Ltd. Nafion solution (5 wt%) and Nafion 117 and 212 PEMs were obtained from DuPont. Ultrapure water (18.2 MΩ) was obtained from a Milli-Q system. High-purity argon gas (Ar, 99.9999%), high-purity hydrogen gas (H_2, 99.9999%) and carbon dioxide (CO_2, 99.999%) were purchased from Hua er wen Gas, Ltd.

Characterization

Powder XRD patterns were collected on a SmartLab-SE X-ray diffractometer (Rigaku) and a Philips PW-1830 X-ray diffractometer with Cu Kα radiation. Catalyst morphology was studied using a Hitachi New Generation SU8010 field-emission SEM. The nanostructure was verified by cryogenic-scanning transmission electron microscopy visualization employing a Gatan 698 cryo-transfer holder and TEM (FEI Talos-S), which was used to avoid the influence of the conventional electron beam on the state of the lead. Samples were kept stable by liquid nitrogen freezing at −180 °C. All cryo-TEM images were taken at cryogenic temperature (−180 °C). TEM images were collected on a Talos F200X microscope provided by the Analytical and Testing Center of Huazhong University of Science. The ion chromatography curve was collected on an 881 Compact IC Pro. Orbitrap liquid chromatography–mass spectrometry (Q Exactive) was used to obtain mass spectra. XPS was conducted on an AXIS-ULTRA DLD-600 W spectrometer with a monochromatic Al Kα source and a charge neutralizer. Binding energies were determined by the C 1*s* spectrum as a reference at 284.8 eV. Raman spectra were recorded on a confocal Raman spectrometer (Alpha300, WITec) using a 532 nm laser source. Multiple spectra were collected for each potential. Contact angle measurements were carried out using an OCA20 contact angle goniometer (Dataphysics). Ultraviolet-visible absorption spectra were collected on a SHIMADZU SolidSpec-3700 spectrometer. Atomic force microscopy images were collected on a scanning probe microscope (SPM-9700). O-K-edge and near-edge X-ray absorption fine-structure spectra were collected on a BL12B X-ray magnetic circular dichroism (XMCD) at the National Synchrotron Radiation Laboratory (NSRL).

Preparation of recycled Pb catalyst

All catalysts used were ecofriendly, being derived from used lead–acid batteries that sourced from either natural waste electric bicycles or simulation of a battery that fails by charging and discharging a current of 30 mA, with a charge–discharge cut-off voltage of 4.8 and 4.0 V, at the LAND testing station. We could then obtain the lead plate by disassembling the waste lead–acid battery and washing it three times with deionized water. This plate was then dried in a vacuum oven for 10 h and subjected to the next procedure of removing the grid from the plate. The prerecycled Pb catalyst was obtained by grinding the above material manually in a mortar for 10 min. Finally r-Pb was obtained by ball milling the prerecycled Pb in a ball mill for 0, 10, 20, 30, 40 and 50 min.

Preparation of working electrode

A PTFE emulsion (1 wt%) was first sprayed on the gas diffusion layer (GDL) to prevent electrowetting during the electrocatalytic process. A homogeneous catalyst ink was first prepared by blending 20 mg of catalyst, 20 µl of 1 wt% PTFE emulsion, 3 ml of ethanol and 100 µl of Nafion solution (5% in ethanol), followed by sonication for 0.5 h. The ink was then air-brushed onto either a GDL (YLS-30T GDL) or PTFE membrane (required for the addition of carbon nanotubes, which account for 30 wt% of catalyst weight, to the ink) as the cathode electrode with a mass loading of 2 mg cm^{-2}. Before using the PTFE membrane, the catalyst-loaded side required to be treated with sodium naphthalene solution for 30 s to increase adhesion between its surface and the catalyst.

In situ SR–FTIR spectroscopy

In situ SR–FTIR measurements were performed at the infrared beamline BL01B of the NSRL through a home-made, top-plate cell reflection infrared set-up with a ZnSe crystal as the infrared transmission window (cut-off energy roughly 625 cm^{-1}). This end station was equipped with an FTIR spectrometer (Bruker66 v/s) with a KBr beam splitter and various detectors (a liquid nitrogen-cooled mercury cadmium telluride detector was used), coupled with an infrared microscope (Bruker Hyperion 3000) with a ×16 objective, and provided infrared spectroscopy measurements with a broad range of 400–4,000 cm^{-1} and high spectral resolution of 0.25 cm^{-1}. The catalyst electrode was tightly pressed against the ZnSe crystal window with a micrometre-scale gap to reduce the loss of infrared light. To ensure the quality of the obtained SR–FTIR spectra, the apparatus adopted a reflection mode with a vertical incidence of infrared light. Each infrared absorption spectrum was acquired by averaging 514 scans at a resolution of 2 cm^{-1}. All infrared spectral acquisitions were carried out following application of a constant potential to the electrode for 20 min. The background spectrum of the catalyst electrode was acquired at an open-circuit voltage before each systemic measurement, and the measured potential range of the electrochemical reaction ranged from −1.0 to −1.8 V versus RHE stepwise.

In situ XAFS measurements

Pb L_3-edge XAFSs were measured at the 1W1B beamline of the Beijing Synchrotron Radiation Facility (BSRF). The storage ring of the BSRF was operated at 2.5 GeV with a maximum electron current of 250 mA. In situ XAFS measurements were performed in a home-made cell. Catalyst powders were dispersed in 500 µl of ethanol, 500 µl of deionized water and 20 µl of Nafion solution (5 wt%, Sigma-Aldrich) and then ultrasonicated for 30 min. Subsequently the evenly distributed catalyst ink was drop-cast onto carbon fibre paper taped with polyimide film on the back to ensure that all electrocatalysts had reacted with the electrolyte. Catalyst-coated carbon fibre paper was used as the working electrode. During XAFS measurements we calibrated the position of the absorption edge (E_0) using Pb foil, and all XAFS data were collected during one period of beam time. Each spectrum was measured three times to ensure the repeatability of the data (all positions of E_0 were almost the same during multiple scans). The position of E_0 is defined as that point corresponding to the maximum value in the derivative curves of the XANES spectra. XAFS raw data were processed according to standard procedures with the Athena module implemented in the Ifeffit software package[37].

In situ Raman spectroscopy

In situ Raman was recorded on a confocal Raman spectroscopy (Alpha300, WITec) using a 532 nm laser source. Measurements were carried out by utilizing a spectroelectrochemical flow cell through a quartz window to detect the cathode GDL. For each measurement, the Raman spectrum was accumulated by two acquisitions (20 s per

acquisition). A syringe pump was used to pump 0.5 M K_2SO_4 (pH 1.0) at a constant flow rate of 3 ml min^{-1} over the GDL. CO_2 gas was introduced to the rear of the GDL. Working electrodes were formed from an air-brushed r-Pb catalyst deposited on a piece of GDL (2 × 2 cm^2, loading mass 2.0 mg cm^{-2}). Potentials were applied (in potential holds) with respect to an Ag/AgCl reference electrode and are reported with respect to RHE. To remain consistent with electrolysis measurements, Raman spectra were obtained 5 min following initial application of the potential. Potential-dependent spectra were obtained at the open-circuit potential and −1.2 to −1.8 V versus RHE. Pt foil was used as the counter electrode.

In situ XRD experiment

In situ XRD for investigation of the phase evolution of the electrode during the charging process was characterized with a 9 kW Rigaku SmartLab machine with Cu Kα radiation (λ = 1.5406 Å) under a scanning speed of 5° min^{-1} and step size 0.02°. The electrode was prepared by mixing 0.7 g of electrode materials, 0.2 g of acetylene black and 0.1 g of polyvinylidene difluoride in 9.0 ml of *N*-methyl pyrrolidone (NMP). Circular carbon cloth (diameter 1.0 cm) was used as the current collector. The obtained slurry was coated onto a carbon cloth and dried at 80 °C for 12 h. The active material was used as a working electrode in the three-electrode set-up. Platinum wire and a saturated calomel electrode were employed as the counter and reference electrode, respectively. CO_2-saturated 0.5 M $KHCO_3$ solution was used as an electrolyte.

Assembly and testing of the PEM reactor

All electrochemical measurements were carried out on a Gamry reference 3000 electrochemical workstation. The CO_2RR catalytic activity of different samples was investigated using a home-made PEM cell with a single room. This electrolyser (the area of electrode exposed was 1 × 1 cm^2) is a two-electrode system with elimination of the reference electrode, in which one GDL loaded with cathode catalyst and another loaded with Pt-Ru black were used as the working and counter electrode, respectively. A Nafion 212 membrane was used as the PEM in the PEM reactor. During the cathode reaction, the rear of the gas diffusion electrode was permeated with high-purity CO_2 at a flow rate of 20.0 sccm, which was controlled using a gas flowmeter during electrolysis. The cathode electrolyte flows over the surface of the catalyst. The pH of the cathode electrolyte was adjusted with H_2SO_4 and KOH and the concentration of potassium ions was maintained at 1 M. In the anode reaction (HOR) the rear of the gas diffusion electrode was permeated with high-purity humid hydrogen at a flow rate of 20.0 sccm, which was controlled using a gas flowmeter during electrolysis. Gas products were analysed by gas chromatograph (Shimadzu GC-2014 and PANNA A91) equipped with PLOT Mol Sieve 5A and Q-bond PLOT columns, and the liquid product was quantitatively analysed with a 400 MHz ^{1}H-nuclear magnetic resonance (NMR) spectrometer using the internal standard method. In the stability test, 300 µl of diluted PTFE emulsion was sprayed on the back of carbon paper every 200 h. Specifically, the PEM device was stopped every 200 h and the GDL electrode removed from the PEM electrolyser. Next, 300 µl of diluted PTFE emulsion was sprayed on the rear of the GDL with a spray gun powered by an air pump. PTFE diluent was prepared with 5 µl of 60% PTFE dispersion and 300 µl of deionized water. The rate of spraying was controlled at 30 µl min^{-1}. Following PTFE emulsion spraying, the gas diffusion electrode was dried under an infrared baking lamp and the repaired gas-diffused electrode was then further assembled into the PEM cell for the next stage of stability testing. The scale-up experiment was carried out in a PEM electrolyser on a Gamry reference 3000 electrochemical workstation assembled with a reference 30 K booster. Electrode area was increased to 5 × 5 cm^2, and CO_2 and hydrogen flow rates were adjusted to 300 sccm. The remaining test details are consistent with the above. Without a specific statement, all electrochemical data presented in this work were not corrected by *iR* compensation in the two-electrode system.

Three-electrode experiment in a PEM cell and H-cell

The three-electrode experiment was similar to the PEM test in regard to operation, except for an additional reference electrode of Ag/AgCl (in saturated KCl solution). Measured potentials using the three-electrode set-up were manually 85% compensated in the three-electrode cell. Solution resistance was tested by potentiostatic electrochemical impedance spectroscopy at frequencies ranging from 0.1 Hz to 100 kHz. Gas products were analysed by gas chromatography (Shimadzu GC-2014 and A91, PANNA Instrument) equipped with PLOT Mol Sieve 5A and Q-bond PLOT columns, and the liquid product was quantitatively analysed with a 400 MHz ^{1}H-NMR spectrometer using the internal standard method. H-cell experiments were carried out in a gas-tight, two-compartment H-cell separated by a Nafion 117 membrane under ambient conditions. Platinum gauze and an Ag/AgCl electrode with saturated KCl solution were used as the counter and reference electrode, respectively. Electrodes prepared with r-Pb were used as the working electrode. CO_2-saturated, 0.5 M K_2SO_4 solution (pH 1.0) was used as the electrolyte, which was stirred at a rate of 600 rpm during electrolysis.

Isotope-labelling experiment

All isotope-labelling experiments were carried out in a home-made, two-chamber, three-electrode flow cell in which the catholyte was 0.5 M K_2SO_4 (pH 1.0) and the anolyte selected was sulfuric acid solution (pH 1.0). Cathode and anode chambers were separated by a PEM. The front aspect was loaded with a r-Pb catalyst and either a $Pb^{12}CO_3$ or $Pb^{13}CO_3$ gas diffusion electrode. The Pb electrode, platinum sheets and Ag/AgCl (in saturated KCl solution) electrodes were used as the working, auxiliary and reference electrode, respectively. The anode and catholyte were both circulated with a peristaltic pump at a flow rate of 20 sccm; the CO_2 gas of $^{12}C^{16}O_2$, $^{13}C^{16}O_2$ and $^{12}C^{18}O_2$ in the cathode reaction was controlled by a flowmeter giving a flow rate of 20 sccm. Potentiostatic electrolysis was then performed at −1.7 V versus RHE and samples were taken at different electrolysis times. Gas products were analysed by online gas chromatography (Shimadzu GC-2014 and A91, PANNA) equipped with a thermal conductivity detector, a methanizer and a flame ionization detector. Argon (99.999% purity) was used as the carrier gas. The liquid product was quantitatively analysed with a 400 MHz ^{1}H-NMR spectrometer using the internal standard method (liquid products were replaced with fresh electrolyte following each sampling). Potentials were measured against an Ag/AgCl reference electrode and converted to the RHE scale by E (versus RHE) = E (versus Ag/AgCl) + 0.22 V + 0.059 × pH.

Mass spectrum test

The reacted carbon paper loaded with the cathode catalyst was rinsed three times with deionized water and then dried overnight in a vacuum-drying box at 60 °C. Next, the carbon paper loaded with the catalyst was soaked in a strong alkaline solution and ultrasonicated for 30 min to dissolve the reacted lead carbonate catalyst and a 50 µm filter membrane was then used to filter out solid impurities to obtain a clear solution containing carbonate, which was detected by liquid-phase mass spectrometry. Before detection, the mass spectrometer injection column was washed three times with deionized water to avoid the interference of residual sampleswith experimental results. Each sample was injected three times and the average value taken.

Ultraviolet-visible spectroscopy experiment

The ultraviolet-visible spectroscopy experiment was conducted to detect hydrogen peroxide produced in a three-electrode flow cell with two chambers and an ultraviolet spectrophotometer. During the test,

Pt-Ru black and IrO_2-supported titanium mesh were used as anode catalysts for HOR and WOR, respectively, in 0.5 M K_2SO_4 (pH 1.0) matches a cathode catalyst of r-Pb. The other four catalysts (480, 520, SKSS and TKK) were loaded on carbon paper for the subsequent WOR experiment. The catholyte was periodically removed during the potentiostatic experiment at −1.7 V versus RHE for subsequent H_2O_2 measurement. H_2O_2 was measured by a traditional cerium sulfate $Ce(SO_4)_2$ titration method based on the mechanism in which a yellow solution of Ce^{4+} is reduced by H_2O_2 to colourless Ce^{3+} (equation (1))[38]. Thus, the concentration of Ce^{4+} before and after the reaction can be measured by ultraviolet-visible spectroscopy. The wavelength used for measurement was 317 nm:

$$2Ce^{4+} + H_2O_2 \rightarrow 2Ce^{3+} + 2H^+ + O_2 \quad (1)$$

Therefore, the concentration of H_2O_2 (M) can be determined by equation (2):

$$M = 2 \times MCe^{4+} \quad (2)$$

where MCe^{4+} is the mole of consumed Ce^{4+}.

Carbonate/CO_2 crossover test

The CO_2 crossover test was based on previous work[7]. We experimented with a three-electrode flow cell at a constant current density of 600 mA cm^{-2} for 6 h, in which an Ag/AgCl electrode and Pt foil were used as the reference and auxiliary electrode, respectively. The CO_2 flow rate was kept constant at 20 sccm using a mass flow controller. The cathode electrolyte contained 1 M K^+, and pH was adjusted by KOH and concentrated H_2SO_4; the anode electrolyte was sealed and collected by an airbag. Gas products collected from the anode were then analysed by gas chromatography.

Techno-economic analysis

Our TEA model follows a general outline reported in a previous work[27,32,39–43], and all parameters are provided in Supplementary Table 2. We explored the costs of producing 100 tonnes of formic acid per day (32,850 tonnes per year, with a capacity factor of 0.9) over a 20 year factory life. We use an experimentally derived PEM full-cell voltage of 2.2 V and an experimentally derived total current density of 600 mA cm^{-2} from our stability experiments to estimate an actual voltage for a prospective industrial electrolyser. Please refer to Supplementary Information for detailed calculations.

DFT calculations

Spin-polarized DFT calculations were performed with periodic slab models using the Vienna Ab initio Simulation Package[44,45]. Electron exchange and correlation interaction were described within the generalized gradient approximation in the Perdew–Burke–Ernzerhof functional[46], and electron–ion interaction was calculated using the projector-augmented wave method with a plane-wave basis set defined by a kinetic energy cut-off of 450 eV[47]. Long-range dispersion interactions between adsorbates and the surface were treated by application of the DFT-D3 method developed by Grimme et al.[48]. The k-point sampling of a 3 × 3 × 1 mesh within the Monkhorst–Pack scheme is utilized for optimization[49]. Geometry optimization and energy calculation were finished when electronic self-consistent iteration and force reached 10^{-5} eV and 0.02 eV $Å^{-1}$, respectively. Bader charge analysis was used to investigate the charge state of atoms in all systems[50].

Free energy change is calculated by the equation $\Delta G = \Delta E + \Delta E_{ZPE} - T\Delta S$, where ΔE is the energy change obtained from DFT calculations, ΔE_{ZPE} is the difference between the adsorbed state and gas and ΔS represents the difference in entropy between the adsorbed state and gas phase. Zero-point energy and entropy are calculated using the vibrational frequencies of intermediate species based on harmonic approximation and fixing the catalyst slabs. In addition, the energy of the proton–electron pair is equal to half the energy of the hydrogen molecule according to the computational hydrogen electrode method[51].

To model the surface of $PbCO_3$ and Pb, we first measured the surface energy of various lattice planes. The lower the surface energy the more stable the corresponding lattice plane. Based on the calculated surface energy shown in Supplementary Fig. 41, we chose stable $PbCO_3$(010) and Pb(111) to represent the surfaces of $PbCO_3$ and Pb metal, respectively. For the Pb(111) surface, a four-layer p(2 × 2) supercell was modelled with three relaxed upper layers and one fixed lower layer. For the $PbCO_3$(010) surface, a two-layer c(1 × 2) supercell was modelled with three relaxed upper layers and 0.5 fixed lower layers. A 15 Å vacuum layer was set along the z direction to avoid periodic interactions.

Data availability

The datasets that support the findings of this study are presented in the text and Supplementary Information. Source data are provided with this paper.

37. Newville, M. IFEFFIT: interactive XAFS analysis and FEFF fitting. *J. Synchrotron Radiat.* **8**, 322–324 (2001).
38. Lu, Z. et al. High-efficiency oxygen reduction to hydrogen peroxide catalysed by oxidized carbon materials. *Nat. Catal.* **1**, 156–162 (2018).
39. Verma, S., Kim, B., Jhong, H. R., Ma, S. & Kenis, P. J. A gross-margin model for defining technoeconomic benchmarks in the electroreduction of CO_2. *ChemSusChem* **9**, 1972–1979 (2016).
40. Ramdin, M. et al. Electroreduction of CO_2/CO to C_2 products: process modeling, downstream separation, system integration, and economic analysis. *Ind. Eng. Chem. Res.* **60**, 17862–17880 (2021).
41. Sisler, J. et al. Ethylene electrosynthesis: a comparative techno-economic analysis of alkaline vs membrane electrode assembly vs CO_2–CO–C_2H_4 tandems. *ACS Energy Lett.* **6**, 997–1002 (2021).
42. Jing, X., Li, F. & Wang, Y. Assessing the economic potential of large-scale carbonate-formation-free CO_2 electrolysis. *Catal. Sci. Technol.* **12**, 2912–2919 (2022).
43. Jin, J. et al. Constrained C_2 adsorbate orientation enables CO-to-acetate electroreduction. *Nature* **617**, 724–729 (2023).
44. Kresse, G. & Furthmüller, J. Efficient iterative schemes for *ab initio* total-energy calculations using a plane-wave basis set. *Phys. Rev. B* **54**, 11169–11186 (1996).
45. Kresse, G. & Hafner, J. *Ab initio* molecular-dynamics simulation of the liquid-metal-amorphous-semiconductor transition in germanium. *Phys. Rev. B* **49**, 14251–14269 (1994).
46. Perdew, J. P., Burke, K. & Ernzerhof, M. Generalized gradient approximation made simple. *Phys. Rev. Lett.* **77**, 3865–3868 (1996).
47. Blochl, P. E. Projector augmented-wave method. *Phys. Rev. B* **50**, 17953–17979 (1994).
48. Grimme, S., Antony, J., Ehrlich, S. & Krieg, H. A consistent and accurate ab initio parametrization of density functional dispersion correction (DFT-D) for the 94 elements H-Pu. *J. Chem. Phys.* **132**, 154104 (2010).
49. Monkhorst, H. J. & Pack, J. D. Special points for Brillouin-zone integrations*. *Phys. Rev. B* **13**, 5188–5192 (1976).
50. Tang, W., Sanville, E. & Henkelman, G. A grid-based Bader analysis algorithm without lattice bias. *J. Phys. Condens. Matter* **21**, 084204 (2009).
51. Nørskov, J. K. et al. Trends in the exchange current for hydrogen evolution. *J. Electrochem. Soc.* **152**, J23 (2005).

Acknowledgements This work is financially supported by National Science Foundation for Distinguished Young Scholars (no. 22325901), the National Key Research and Development Program of China (nos. 2021YFA1600800 and 2021YFA1501000), the National Natural Science Foundation of China (no.22075092), the Program for HUST Academic Frontier Youth Team (nos. 2018QYTD15 and 2019QYTD11), the Huazhong University of Science and Technology–Queen Mary University of London Strategic Partnership Research Funding (no. 2022-HUST-QMUL-SPRF-03) and the Innovation and Talent Recruitment Base of New Energy Chemistry and Device (no. B21003). We thank beamline BL01B (for finfrared spectroscopy and microspectroscopy) and BL12B X-ray magnetic circular dichroism (XMCD) at NSRL and beamline 1W1B (XAFS) at BSRF. We thank BL20U and BL14W1 at the Shanghai Synchrotron Radiation Facility for providing the beam time. The computational study is supported by Marsden Fund Council from Government funding (no. 21-UOA-237) and a Catalyst: Seeding General Grant (no. 22-UOA-031-CGS), managed by Royal Society Te Apārangi. Z.W. and R.L. acknowledge the use of New Zealand eScience Infrastructure high-performance computing facilities, consulting support and/or training services as part of this research. We acknowledge the support of WNLO of HUST and the Analytical and Testing Center of Huazhong University of Science and Technology for XRD, XPS, Raman, SEM, TEM, FTIR, inductively coupled plasma–mass spectrometry and NMR measurements. We also thank L. Zhuang at Wuhan University, J. L. Gong at Tianjin University, D. F. Gao at the Dalian Institute of Chemical Physics and J. J. Ge at the University of Science and Technology of China for fruitful discussions.

Author contributions B.Y.X. conceived and supervised the project. W.F. and B.Y.X. designed and carried out electrochemical experiments. R.L. carried out DFT calculations. Z.W. and B.Y.X. supervised and advised on DFT calculations. W.F., X.L., S.W., F.S., T.Y. and B.Y.X. performed and discussed soft X-ray absorption spectroscopy characterization. W.F., D.W., X.Y. and T.Y. assisted with in situ FTIR experiments. C.H. assisted with ultraviolet experiments. W.F., Y.L. and T.Z. helped with the in situ Raman test. W.G., F.M.L., C.X., Y.Y. and H.N. contributed to results discussion and data analysis. Y.Z. contributed to XPS result discussion. L.D. provided in situ XRD measurements. W.G., Y.M., C.Z., Y.P., G.W., X.G., B.Y. and B.T. commented on and revised the manuscript. W.F., R.L., T.Y., Z.W. and B.Y.X. wrote and revised the manuscript. All authors discussed the results and assisted with manuscript preparation. W.F., W.G. and R.L. contributed equally to this work.

Competing interests The authors declare no competing interests.

Additional information

Supplementary information The online version contains supplementary material available at https://doi.org/10.1038/s41586-023-06917-5.

Correspondence and requests for materials should be addressed to Tao Yao, Ziyun Wang or Bao Yu Xia.

Peer review information *Nature* thanks Quan-Hong Yang, Mahbub Islam and the other, anonymous, reviewer(s) for their contribution to the peer review of this work.